



<b>Publication Year</b>	2015
<b>Acceptance in OA</b>	2020-03-18T16:05:02Z
<b>Title</b>	Disentangling dark sector models using weak lensing statistics
<b>Authors</b>	GIOCOLI, CARLO, Metcalf, R. Benton, BALDI, MARCO, MENEGHETTI, MASSIMO, MOSCARDINI, LAURO, Petkova, Margarita
<b>Publisher's version (DOI)</b>	10.1093/mnras/stv1473
<b>Handle</b>	<a href="http://hdl.handle.net/20.500.12386/23360">http://hdl.handle.net/20.500.12386/23360</a>
<b>Journal</b>	MONTHLY NOTICES OF THE ROYAL ASTRONOMICAL SOCIETY
<b>Volume</b>	452

# Disentangling dark sector models using weak lensing statistics

Carlo Giocoli,<sup>1,2,3,4\*</sup> R. Benton Metcalf,<sup>1</sup> Marco Baldi,<sup>1,2,3</sup> Massimo Meneghetti,<sup>2,3,5</sup>  
Lauro Moscardini<sup>1,2,3</sup> and Margarita Petkova<sup>6</sup>

<sup>1</sup>*Dipartimento di Fisica e Astronomia, Alma Mater Studiorum Università di Bologna, viale Bertini Pichat, 6/2, I-40127 Bologna, Italy*

<sup>2</sup>*INAF-Osservatorio Astronomico di Bologna, via Ranzani 1, I-40127 Bologna, Italy*

<sup>3</sup>*INFN-Sezione di Bologna, viale Bertini Pichat 6/2, I-40127 Bologna, Italy*

<sup>4</sup>*Aix Marseille Université, CNRS, LAM (Laboratoire d'Astrophysique de Marseille) UMR 7326, F-13388 Marseille, France*

<sup>5</sup>*Jet Propulsion Laboratory, 4800 Oak Grove Dr. Pasadena, CA 91109, USA*

<sup>6</sup>*Department of Physics, Ludwig-Maximilians-Universität, Scheinerstr. 1, D-81679 München, Germany*

Accepted 2015 July 1. Received 2015 June 10; in original form 2015 February 11

## ABSTRACT

We perform multiplane ray tracing using the GLAMER gravitational lensing code within high-resolution light-cones extracted from the CoDECS simulations: a suite of cosmological runs featuring a coupling between dark energy and cold dark matter (CDM). We show that the presence of the coupling is evident not only in the redshift evolution of the normalization of the convergence power spectrum, but also in differences in non-linear structure formation with respect to  $\Lambda$ CDM. Using a tomographic approach under the assumption of a  $\Lambda$ CDM cosmology, we demonstrate that weak lensing measurements would result in a  $\sigma_8$  value that changes with the source redshift if the true underlying cosmology is a coupled dark energy (cDE) one. This provides a generic null test for these types of models. We also find that different models of cDE can show either an enhanced or a suppressed correlation between convergence maps with differing source redshifts as compared to  $\Lambda$ CDM. This would provide a direct way to discriminate between different possible realizations of the cDE scenario. Finally, we discuss the impact of the coupling on several lensing observables for different source redshifts and angular scales with realistic source redshift distributions for current ground-based and future space-based lensing surveys.

**Key words:** gravitational lensing: weak – methods: numerical – galaxies: haloes – cosmology: theory – dark matter.

## 1 INTRODUCTION

It is now widely accepted by the scientific community that the energy content of our Universe must be largely dominated by some unknown particles and fields beyond the standard model of particle physics. These are characterized by extremely weak interactions with the electromagnetic field, and are thereby termed the ‘dark’ components of the Universe (Suzuki et al. 2012; Planck Collaboration XVI 2013), and generically classified as ‘dark matter’ and ‘dark energy’ (DE) based on their background and clustering properties. While DE is supposed to source the observed accelerated cosmic expansion (Riess et al. 1998; Schmidt et al. 1998; Perlmutter et al. 1999; Kowalski et al. 2008) and to have at most weak spatial density fluctuations, dark matter constitutes more than 80 per cent of the clustering mass in the Universe and drives the growth of cosmic structures (Lacey & Cole 1993; Tormen 1998; Springel et al. 2005;

Giocoli et al. 2007) as well as the deflection of light rays as predicted by general relativity (Bartelmann & Schneider 2001; Bartelmann 2010). The latter phenomenon is known as ‘gravitational lensing’: the light travelling from background sources (such as distant galaxies) down to the observer is deflected by the inhomogeneous intervening matter distribution, causing a distortion of light bundles and consequently a modification of the observed galaxy shape (Kaiser & Squires 1993; Kaiser, Squires & Broadhurst 1995). Depending on the overall magnitude of the light deflection we can distinguish between two main regimes of gravitational lensing: the strong lensing (SL) characterizing the large distortions generated by single highly overdense regions of the Universe (as the central regions of galaxies and galaxy clusters) and the weak lensing (WL) that occurs as the integrated effect of light rays travelling through the inhomogeneous cosmic web (Meneghetti et al. 2005; Kneib & Natarajan 2011). In particular, weak gravitational lensing represents an important and widely used tool for cosmological investigation and to probe the matter density around galaxies and galaxy clusters (Mandelbaum et al. 2006; Okabe et al. 2010; Oguri et al. 2012). However, as this

\* E-mail: carlo.giocoli@lam.fr

effect is weak – by definition – it is necessary to average over a large area of sky in order to extract a statistically significant lensing signal.

In the present work, we will focus on the prospects for using WL as a cosmological probe to distinguish among different models of DE. By analysing the distorted shape of background galaxies as a function of their redshift, WL can in principle constrain the total matter density of the Universe,  $\Omega_m$ , the linear matter power spectrum normalization,  $\sigma_8$  and the DE equation of state  $w_{DE}$ . Furthermore, this could reveal possible signatures of an interaction between the two dark components (Beynon et al. 2012; Carbone et al. 2013; Pace et al. 2015). In order to achieve such discriminating power, however, highly accurate and unbiased shear measurements – as the ones expected for the next generation of wide surveys – will be required. Since gravitational lensing does not depend on the bias between the distributions of dark and luminous matter, it represents a complementary probe to other constraining observations like supernovae, baryon acoustic oscillations and cosmic microwave background (CMB) measurements (Kilbinger et al. 2013; Kilbinger 2014).

In recent years, the activities of the CFHTLenS collaboration have greatly contributed to measuring the cosmic shear signal in different patches of the sky with the aim to constrain cosmological parameters. From the first exploration by Fu et al. (2008) of WL by large-scale structure in the linear regime on a region of  $57 \text{ deg}^2$ , the CFHTLenS work has progressed through a series of different steps (Benjamin et al. 2013; Kilbinger et al. 2013) and improvements (Hildebrandt et al. 2012; Heymans et al. 2012, 2013) before performing a full WL measurement in three dimensions using a spherical harmonic approach (Kitching et al. 2014). As demonstrated by the shape measurement of galaxies in the COSMOS field observed by the *Hubble Space Telescope* (Amara et al. 2012), in the near future, WL space-based measurements (Refregier, Rhodes & Groth 2002; Refregier et al. 2004) combined with other independent probes of the large-scale matter distribution will be able to discriminate with high accuracy among various possible scenarios for the fundamental constituents of the dark sector (Harnois-Déraps et al. 2015; Kitching, Heavens & Das 2015). Finally, WL is also a promising tool for identifying clusters (Maturi et al. 2005) in blank fields, complementing and possibly driving other independent approaches (Bellagamba et al. 2011).

Ray tracing through light-cones extracted from numerical simulations represents the most accurate method to compute WL predictions (Hilbert et al. 2008). In particular, this is the case for cosmologies that have not yet been fitted to semi-analytical prediction tools for their behaviour in the non-linear regime (Lewis, Challinor & Lasenby 2000; Takahashi et al. 2012). The drawback of this approach is that it is computationally demanding as it requires to sample the full cosmological parameter space with a series of  $N$ -body simulations. However, high-speed computers and improvements of numerical solver algorithms are progressively simplifying the ray-tracing methodology.

Studying the WL signal as a function of source redshift is commonly called ‘lensing tomography’ and is likely to have great significance for cosmology in the future (Schrabback et al. 2010). This is the technique we will investigate in the present work with the aim of understanding whether a tomographic slicing of background sources might increase the information extracted from WL observables on possible interactions between dark matter and DE. In particular, the possibility of fully exploiting this method to measure specific DE signatures does not only rely on a high accuracy of the shear

measurements, but also on a high source density which is necessary to reduce statistical errors.

The CoDECS cosmological simulations are hydrodynamical simulations but do not include gas cooling, star formation and the feedback mechanism of the baryonic component, which may imprint a non-negligible signal in the cosmic shear power spectrum on angular scales smaller than a few arcminutes (Semboloni, Hoekstra & Schaye 2013; Fedeli et al. 2014; Harnois-Déraps et al. 2015). However, as we are interested in examining relative differences of the coupled dark matter–DE models with respect to the standard  $\Lambda$  cold dark matter ( $\Lambda$ CDM) one we will make the common assumption that the relative differences between models would be only weakly affected by baryonic physics. This assumption is also reinforced by the fact that the baryonic physics has a non-negligible impact for scale  $k \gtrsim 3500 h \text{ Mpc}^{-1}$ .

Pace et al. (2015) have already performed ray-tracing simulations in different coupled dark matter–DE models extracted from the CoDECS suite, constructing maps for different lensing quantities starting from the lensing potential. Their analysis is performed on maps with a resolution of around 20 arcsec and considering sources located at redshift  $z_s = 1$ . They found that the most significant differences from the standard  $\Lambda$ CDM model are due to differences in the growth of the perturbations and to the effective friction term in non-linear dynamics. The most extreme realization of coupled dark energy (cDE) expectedly showed the largest difference from  $\Lambda$ CDM of about 40 per cent in the power spectrum, as found also by Carbone et al. (2013). In this paper, we extend and complement their analyses focusing the attention on the small-scale regime thanks to high-resolution ray-tracing simulations performed with the GLAMER code. In addition, we construct ray-tracing simulations considering different source redshift distributions, with the aim of tomographically evaluate the difference between cDE models and the standard  $\Lambda$ CDM one.

The structure of this paper is organized as follows. In Section 2, we summarize the numerical simulations that are used to construct the light-cones and in Section 3 we describe the methodology we adopted to perform multiplane ray tracing. Results and lensing statistical analyses are presented in Section 4. Finally, in Section 5 we discuss our conclusions and summarize our main results.

## 2 COSMOLOGICAL SIMULATION

For our investigation, we rely on the publicly available CoDECS simulations (Baldi 2012c) that represent the largest suite of cosmological and hydrodynamical simulations of cDE models to date. The simulations have been performed by means of a modified version developed by Baldi et al. (2010), of the widely used TREEPM/Smoothed-Particle Hydrodynamics  $N$ -body code GADGET (Springel 2005), and self-consistently include all the effects associated with the non-minimal interaction between a DE scalar field  $\phi$  and CDM particles. The CoDECS suite includes several different possible combinations of the scalar DE potential – the exponential (Lucchin & Matarrese 1985; Wetterich 1988) or the SUGRA (Brax & Martin 1999) potentials for example – and of the coupling function which can be either constant or exponential in the scalar field (see e.g. Baldi et al. 2011a). In the present work, we will consider four models ( $\Lambda$ CDM, EXP003, EXP008e3 and SUGRA003) with different combinations of these free functions that are summarized in Table 1. For more details on the models, we refer to Baldi (2012c).

Such variety of scenarios is reflected in the diversity of effects that they determine on both the background expansion history and the linear and non-linear evolution of perturbations. More

**Table 1.** The list of cosmological models considered in the present work and their specific parameters. All the models have the same amplitude of scalar perturbations at  $z_{\text{CMB}} \approx 1100$ , but have different values of  $\sigma_8$  at  $z = 0$ . In short,  $\alpha$  is a parameter in the inflation potential as shown,  $\beta(\phi)$  is the coefficient of the coupling term with dark matter density and  $w_\phi(z = 0)$  is the effective equation of state parameter ( $p/\rho$ ). See Baldi (2012c) for details.

Model	Potential	$\alpha$	$\beta(\phi)$	$w_\phi(z = 0)$	$\sigma_8(z = 0)$
$\Lambda$ CDM	$V(\phi) = A$	–	–	–1.0	0.809
EXP003	$V(\phi) = Ae^{-\alpha\phi}$	0.08	0.15	–0.992	0.967
EXP008e3	$V(\phi) = Ae^{-\alpha\phi}$	0.08	0.4exp[3 $\phi$ ]	–0.982	0.895
SUGRA003	$V(\phi) = A\phi^{-\alpha}e^{\phi^2/2}$	2.15	–0.15	–0.901	0.806

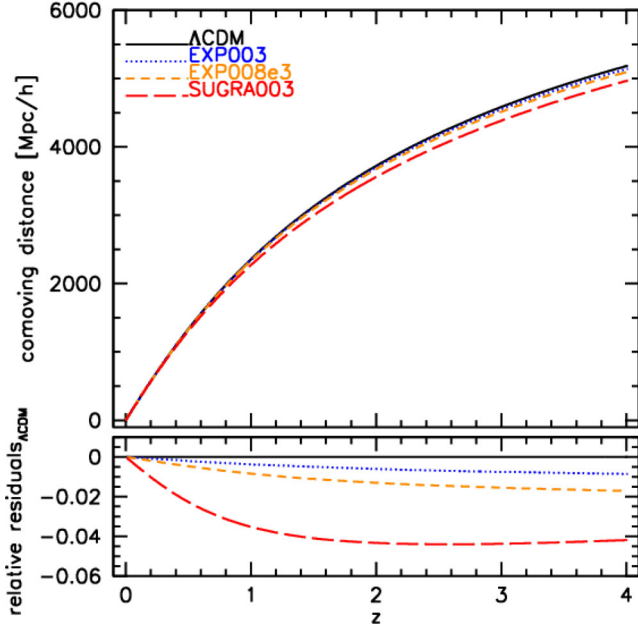


**Figure 1.** Comoving distances as a function of redshifts for the four considered models of the CoDECS suite. The bottom panel shows the relative difference of the models with respect to  $\Lambda$ CDM.

specifically, the dynamical evolution of the DE scalar field through a matter dominated scaling solution alters the cosmic expansion history with respect to the standard  $\Lambda$ CDM cosmology in a way that substantially depends on the potential and coupling functions adopted. This is shown in Fig. 1, where we show the comoving distance as a function of redshift for the four models. The bottom panel displays the relative differences of the comoving distances at a given redshift between the cDE models and the reference  $\Lambda$ CDM. From the figure, we can notice that while locally the comoving distances are consistent with each other (due to the same normalization of Hubble parameter,  $H_0$ , for all the cosmologies), at higher redshifts the cDE models have smaller volumes than  $\Lambda$ CDM, with a maximum effect for the SUGRA003 cosmology that deviates low from  $\Lambda$ CDM by about 5 per cent already at  $z = 2$ .

At the level of linear density perturbations, the models all predict an enhanced growth rate with respect to  $\Lambda$ CDM at high redshifts. However, while the EXP003 and the EXP008e3 models show an enhanced growth also at low redshifts, thereby resulting in a larger value of  $\sigma_8$  at  $z = 0$ , the SUGRA003 cosmology is characterized by a slower growth as compared to  $\Lambda$ CDM for  $z \lesssim 7$  resulting in a comparable value of  $\sigma_8$  (see the last column of Table 1). The non-linear effects of these models have been studied in several

publications based on the outcomes of the CoDECS simulations and range from the impact of cDE on the abundance and structural properties of haloes (Baldi, Lee & Macciò 2011b; Baldi 2012a; Cui, Baldi & Borgani 2012; Giocoli et al. 2013), on the statistical properties of the large-scale structures distribution (Marulli, Baldi & Moscardini 2012; Moresco et al. 2014), on the properties of the inter-galactic medium at high redshifts (Baldi & Viel 2010) and on WL statistics (Beynon et al. 2012; Carbone et al. 2013; Pace et al. 2015). In the present work, we aim at extending the latter analysis by investigating whether a tomographic slicing of the background sources within the light-cone of a 25 deg<sup>2</sup> field of view might provide additional information to observationally distinguish the cDE models from the standard  $\Lambda$ CDM cosmology and possibly the different cDE models from each other.

For our analysis, we will make use of the L-CoDECS series consisting of a periodic cosmological box of 1 Gpc  $h^{-1}$  aside filled with  $2 \times 10^{24}$  particles evolved through collisionless dynamics from  $z = 99$  to  $z = 0$ . All the models share the same initial conditions at the redshift of the CMB  $z_{\text{CMB}} \approx 1100$  and have the same cosmological parameters at  $z = 0$  consistent with the WMAP7 cosmological results (Komatsu et al. 2011), namely  $\Omega_{\text{CDM}} = 0.226$ ,  $\Omega_{\text{DE}} = 0.729$ ,  $h = 0.703$ ,  $A_s = 2.42 \times 10^{-9}$ ,  $\Omega_b = 0.0451$  and  $n_s = 0.966$ . The mass resolution is  $M_{\text{CDM}}(z = 0) = 5.84 \times 10^{10} M_\odot h^{-1}$  for CDM particles and  $M_b = 1.17 \times 10^{10} M_\odot h^{-1}$  for the (collisionless) baryonic particles (see Baldi 2012c, for a detailed discussion), while the gravitational softening was set to  $\epsilon_g = 20$  kpc  $h^{-1}$ .

### 3 LENSING PIPELINE

In the following sections, we will present the procedure we followed in constructing the lens planes from the cosmological simulations, assembling them into light-cones and tracing the paths of light through them.

#### 3.1 Constructing the light-cone: MAPSIM

Our code for extracting the particles from the simulation’s snapshot files and assembling them into a light-cones is called MAPSIM. The steps MAPSIM goes through in constructing a light-cone can be summarized as follows:

(i) Read in an input parameter file that contains information about the desired field of view, highest source redshift (in this case taken to be  $z_s = 4$ ) and locations of snapshot files. The number of lens planes required is decided ahead of time in order to avoid gaps in the constructed light-cone. The choice  $z_s = 4$  has been made to better understand where the dynamical evolution of the DE scalar field and the enhanced growth rate – in the different models – start to leave a mark in the WL observables. Notice that at low redshifts the

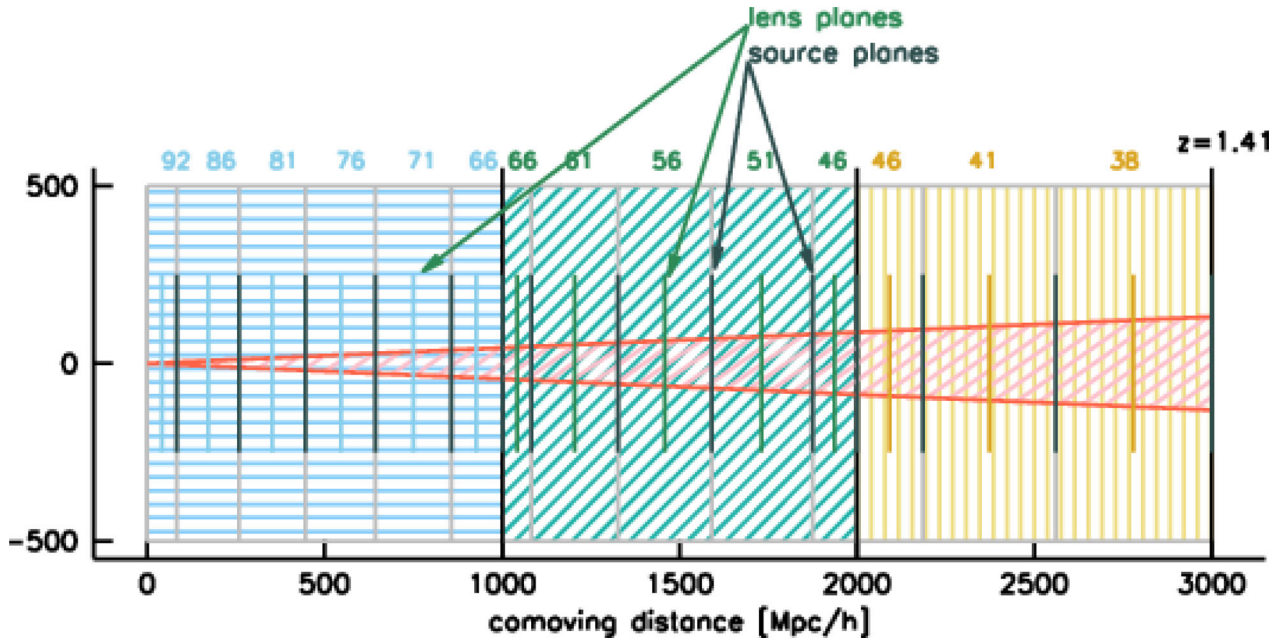


**Figure 2.** An illustration of the construction of the light-cone up to redshift  $z = 1.4$  with an aperture of  $5 \times 5 \text{ deg}^2$  for the  $\Lambda\text{CDM}$  model. The light-cone passes through three simulation boxes, since the comoving distance corresponding to  $z = 1.4$  is  $3 \text{ Gpc } h^{-1}$ . As indicated in the upper part of the figure we have 12 snapshots available up to this considered source redshift from which we construct 14 lens planes. In the square that contains a single simulation box we stack together slices from difference snapshots of the box. The snapshot id numbers are shown on the top of each rectangle representing the slices. The different colours used to shade the squares indicate that the simulation boxes have been randomized as described in Roncarelli et al. (2007). The pink shaded triangle shows the region of the simulation snapshots used to construct the planes within the light-cones.

models show a different behaviour: while EXP003 and EXP008e3 continue their enhanced growth, SUGRA003 does not.

(ii) Read in each snapshot file going from the present time to higher redshift snapshots while extracting only the particle positions within the desired field of view. Only a single snapshot is in memory at any time.

(iii) Selection and randomization of each snapshot is done as in Roncarelli et al. (2007). If the light-cone reaches the border of a simulation box before it has reached a redshift range where the next snapshot will be used, the box is rerandomized and the light-cone extended through it again.

(iv) The lensing planes are built by mapping the particle positions to the nearest pre-determined plane, maintaining angular positions, and then pixelizing the surface density using the triangular-shaped cloud method (Hockney & Eastwood 1988). The grid pixels are chosen to have the same angular size on all planes. The lens planes have been constructed each time a piece of simulation is taken from the stored particle snapshots; their number and frequency depend on the number of snapshots stored while running the simulation.

In Fig. 2, we show an illustration of the construction of the light-cone up to redshift  $z = 1.4$ , for the  $\Lambda\text{CDM}$  model, piling one on top of the others the different portions of the simulation snapshots. The differently coloured squares are different realizations using the same randomization method. The rectangles within the squares represent the portion of the simulation snapshot from which the particle density distributions have been taken. The number on the top of them are the id numbers of the corresponding simulation snapshots. The vertical line in the middle of each rectangle indicates the planes on to which the particles are projected for ray shooting. We remind the reader that to save disc space not all 92 simulation snapshots have been stored in running the simulation. Up to redshift

**Table 2.** Comoving distances in  $\text{Mpc } h^{-1}$  for three different source redshifts in the considered cosmological models.

Model	$z_s = 0.5$	$z_s = 1.4$	$z_s = 4$
$\Lambda\text{CDM}$	1327.27	3000	5179.52
EXP003	1324.56	2999.75	5135.05
EXP008e3	1320.86	2981.97	5091.15
SUGRA003	1297.07	2892.85	4962.47

$z_s = 4$ , we saved 18 snapshots which are sufficient to consistently model the matter density distribution in our light-cones.

The maps were constructed with a  $5 \times 5 \text{ deg}^2$  field of view and an angular resolution of 8.8 arcsec. For each model, we have constructed 25 independent realizations, being careful that in each realization the same field of view is selected in the different cosmologies. However, considering the different comoving distance–redshift evolution through the simulation snapshots we have built 22 planes up to redshift  $z = 4$  for the  $\Lambda\text{CDM}$ , EXP003 and EXP008e3, while we have 21 planes for the SUGRA003 model. In Table 2, we point out the comoving distances corresponding to redshift  $z_s = 0.5$ , 1.4 and 4 for the four models.

### 3.2 Ray tracing through the planes

Once the lens planes are created as described in the previous section the lensing calculation itself is done using the GLAMER lensing code (Metcalf & Petkova 2014; Petkova, Metcalf & Giocoli 2014). The multiplane ray-tracing method is described in detail in Petkova et al. (2014) so we will only outline the procedure here.

A few definitions are required. If the angular position on the sky is  $\theta$  and the position on the source plane expressed as an angle (the

unlensed position) is  $\boldsymbol{\beta}$ , then a distortion matrix  $\mathbf{A}$  can be defined as

$$\mathbf{A} \equiv \frac{\partial \boldsymbol{\beta}}{\partial \boldsymbol{\theta}} = \begin{pmatrix} 1 - \kappa - \gamma_1 & \gamma_2 - \gamma_3 \\ \gamma_2 + \gamma_3 & 1 - \kappa + \gamma_1 \end{pmatrix}. \quad (1)$$

The traditional decomposition of this matrix is shown, where  $\kappa$  is called the convergence and  $\boldsymbol{\gamma}$  represents the shear. The torsion,  $\gamma_3$ , represents a rotation which can occur when there are multiple deflection planes. It is of order the shear squared (see Petkova et al. 2014) and according to our numerical calculations, and those of Becker (2013), it is quite small, but it will be retained here for completeness.

When there is a single lens plane, the convergence can be expressed as a dimensionless surface density,

$$\kappa(\boldsymbol{\theta}) \equiv \frac{\Sigma(\boldsymbol{\theta})}{\Sigma_{\text{crit}}}, \quad (2)$$

where

$$\Sigma_{\text{crit}} \equiv \frac{c^2}{4\pi G} \frac{D_l}{D_s D_{ls}} \quad (3)$$

is called the critical density,  $c$  is the speed of light,  $G$  is Newton's constant and  $D_l$ ,  $D_s$  and  $D_{ls}$  are the angular diameter distances between observer–lens, observer–source and source–lens, respectively. In general, with multiple lens planes, this is not the case however.

The deflection caused by a lens plane,  $\boldsymbol{\alpha}$ , is related to the surface density on the plane,  $\Sigma(\mathbf{x})$ , through the differential equations

$$\nabla^2 \phi(\mathbf{x}) = \frac{4\pi G}{c^2} \Sigma(\mathbf{x}), \quad \boldsymbol{\alpha}(\mathbf{x}) = \nabla \phi(\mathbf{x}), \quad (4)$$

where the derivatives are with respect to the position on the lens plane. These equations are solved on each source plane by performing a discrete Fourier transform (DFT) on the density map, multiplying by the appropriate factors and then transforming back to get a deflection map with the same resolution as the density map. With the same DFT method the shear caused by each plane is simultaneously calculated. Since the rays are propagated between planes using the standard distances in a Robertson–Walker metric which assumes a uniform distribution of matter the addition of matter on each of the planes will, in a sense, overcount the mass in the universe. Without correcting for this the average convergence from the planes will be positive and will cause the average distance for a fixed redshift to be smaller than it should be. To compensate for the implicit density between the planes, the ensemble average density on each plane is subtracted. Each plane then has zero convergence on average and the average redshift–distance relation is as it would be in a perfectly homogeneous universe.

After the deflection and shear maps on each plane are calculated the light rays are traced from the observers through the lens planes out to the desired source redshift. The shear and convergence are also propagated through the planes as detailed in Petkova et al. (2014). GLAMER performs a complete ray-tracing calculation that takes into account non-linear coupling terms between the planes as well as correlations between the deflection and the shear. No WL assumption is made at this stage. The rays are shot in a grid pattern with the same resolution as the mass maps:  $5^\circ$  resolved with 2048 pixels on a side.

In Fig. 3, we show the convergence maps of the same light-cone realization extracted from the different models – top left  $\Lambda$ CDM, top right EXP003, bottom left EXP008e3 and bottom right SUGRA003. We show the maps for sources located at three fixed redshifts:  $z_s = 0.5, 1.4$  and  $4$  from top to bottom, respectively. The sticks in

each panel indicate the directions of the corresponding shear field. As discussed in Cui et al. (2012) and Giocoli et al. (2013), we immediately notice that the density distribution differs in cDE models from  $\Lambda$ CDM due to a difference in the growth as a function of redshifts. The top panels show the presence in the field of view of a cluster, at redshift  $z < 0.5$ , which, while it appears ‘assembled’ and with a single peak in the  $\Lambda$ CDM and the SUGRA003 models, it is less evolved, showing multiple components, in EXP003 and EXP008e3. The intermediate- and the high-redshift maps also exhibit differences mainly because of differences in the evolution of the power spectrum normalization and non-linear structure formation.

### 3.3 Analytic methods

An approximation is commonly used to calculate the convergence power spectrum that avoids the complications discussed in the previous two sections. The convergence can be calculated by adding up the single plane convergences, equation (4), along an unperturbed light ray, the Born approximation. This results in the expression

$$\kappa(z_s, \boldsymbol{\theta}) = \frac{3H_0^2 \Omega_m}{2c^2} \int_0^{w(z_s)} dw \frac{D(z)D(z_s)}{D(z_s)a(z)^2} \delta(D(z)\boldsymbol{\theta}, z), \quad (5)$$

where  $w$  is the radial comoving distance,  $a \equiv (1+z)^{-1}$  is the scale factor and  $\delta(\mathbf{x}) \equiv (\rho(\mathbf{x}) - \bar{\rho})/\bar{\rho}$  is the density contrast. The angular power spectrum of  $\kappa$  in the small angle limit is then found to be

$$P_\kappa(l) = \frac{9H_0^4 \Omega_m^2}{4c^4} \int_0^{w_s} dw \left( \frac{D(z_s)}{D(z_s)a(z)} \right)^2 P_\delta \left( l \frac{a(z)}{D(z)}, z \right) \quad (6)$$

(Kaiser 1992). Either an analytic model for the density power spectrum,  $P_\delta(k, z)$ , or a power spectrum taken directly from a simulation can be inserted into equation (6).

In the following sections, we will contrast our direct calculations with some analytic models using this approximation. For some applications, this approximation is adequate, but in new situations and for particular statistics it needs to be checked against simulations.

## 4 RESULTS

### 4.1 Convergence power spectrum

In the real (angular) space, a direct measurement of WL is the two-point shear correlation functions  $\xi_+$  and  $\xi_-$  that can be obtained by averaging over galaxy pairs with angular separations  $|\boldsymbol{\theta}_i - \boldsymbol{\theta}_j|$  within a bin  $\theta$ :

$$\xi_{\pm}(\theta) = \frac{\sum_{ij} w_i w_j [\epsilon_i(\boldsymbol{\theta}_i) \epsilon_i(\boldsymbol{\theta}_j) \pm \epsilon_{\times}(\boldsymbol{\theta}_i) \epsilon_{\times}(\boldsymbol{\theta}_j)]}{\sum_{ij} w_i w_j}, \quad (7)$$

where the measured galaxy ellipticity measurements  $\epsilon_t$  and  $\epsilon_{\times}$  are the tangential and cross-components with respect to the line connecting the pair, respectively. The weights  $w$  are obtained from the galaxy shape measurement pipeline (Bernstein & Jarvis 2002; Bridle et al. 2010; Kacprzak et al. 2012; Miller et al. 2013). These two-point shear correlation functions can be calculated from the convergence power spectrum by the relation:

$$\xi_{+/-} = \frac{1}{2\pi} \int_0^\infty dl P_\kappa(l) J_{0/4}(l\theta), \quad (8)$$

where  $J_0$  and  $J_4$  are the Bessel functions and we have set the B-mode power spectrum to zero because lensing generates only E-modes in the WL limit.

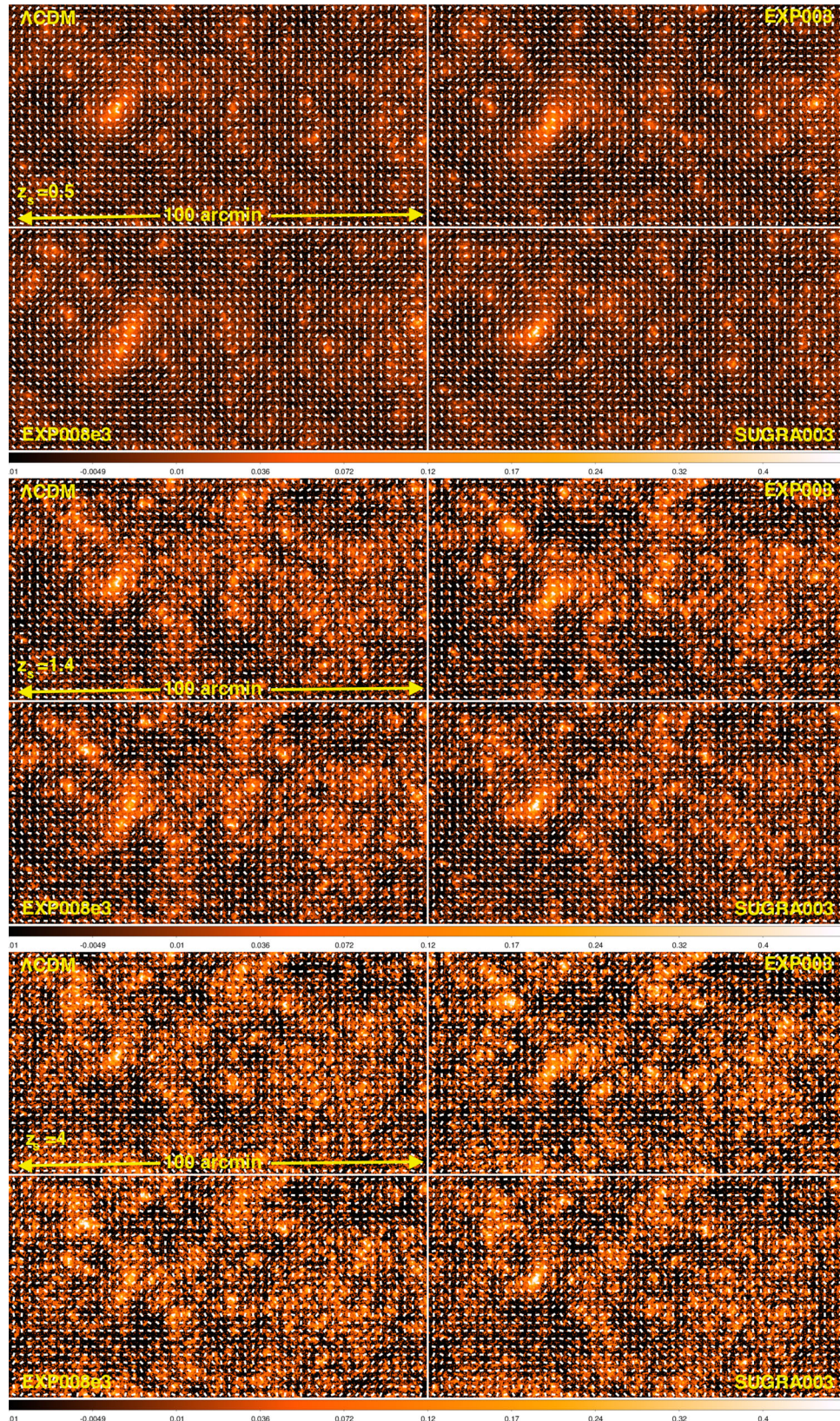


**Figure 3.** Convergence maps of a light-cone with aperture 100 arcmin on the  $x$ -side, for the four considered models – in each panel top left  $\Lambda$ CDM, top right EXP003, bottom left EXP008e3 and bottom right SUGRA003. The three panels refer to different cases: sources located at redshifts  $z_s = 0.5, 1.4$  and 4, from top to bottom, respectively. In each map, the sticks show the direction of the corresponding field.

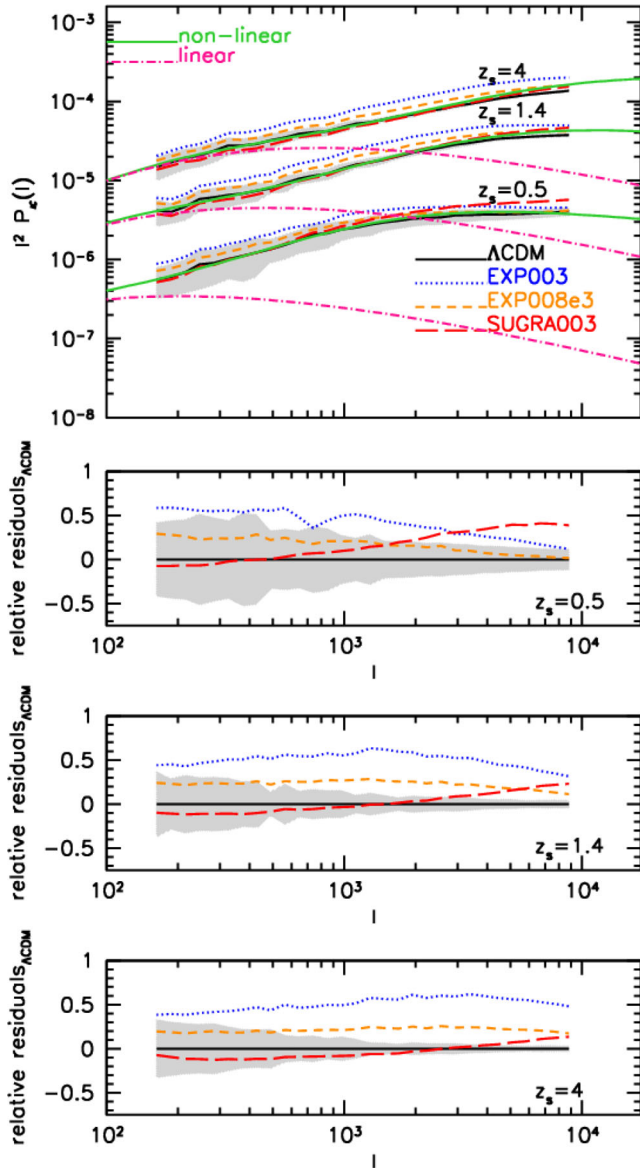


**Figure 4.** Convergence power spectrum of the four considered CoDECS cosmologies for three different source redshifts:  $z_s = 0.5, 1.4$  and  $4$ . The shaded grey region encloses the standard deviation of the mean associated to the  $\Lambda$ CDM model on the different  $5^\circ \times 5^\circ$  light-cone realizations. In the top panel, the solid and dot-dashed curves show the linear and non-linear CAMB predictions for the  $\Lambda$ CDM cosmology, respectively. For the non-linear power spectrum prediction, we adopt the extended version of the Halofit Model (Smith et al. 2003) from Takahashi et al. (2012). In the bottom panels, we present the relative residuals of the convergence power spectra with respect to the  $\Lambda$ CDM cosmology of the three cosmological models – for each of the considered source redshift cases – featuring a direct interaction between the dark energy and dark matter.

In Fig. 4, we show the convergence power spectrum up to  $l \approx 10^4$  measured in the four cosmologies, considering sources at three different redshifts:  $z_s = 0.5, 1.4$  and  $4$ . The curve referring to each model represents the average over all the light-cones. For the  $\Lambda$ CDM case, the shaded region encloses the standard deviation of the mean associated to the different realizations. The  $l_{\min}$  considered corresponds to the minimum resolvable in the assumed field of view. In the same figure, we also show the predictions obtained by inserting into equation (6) analytic models for the linear and

the non-linear power spectrum, namely the Halofit Model (Smith et al. 2003) from Takahashi et al. (2012) implemented in CAMB (Lewis et al. 2000). As shown in Pace et al. (2015) – where they consider the matter density distribution only up to redshift  $z_s = 1$  – the EXP003 model has much more power than the  $\Lambda$ CDM with the largest difference being on small scales and increasing with the source redshift. Interestingly, for the SUGRA003 model, the power spectrum is below  $\Lambda$ CDM for low multipoles and above it for high multipoles. This is a result of the fifth force term in the dark matter–DE coupling which drives rapid structure formation at high redshift, but slows it down at lower redshift. The SUGRA003 and the  $\Lambda$ CDM power spectra intersect at about  $l \sim 10^3$ , slightly decreasing with the source redshifts. From Fig. 4, we also see that the EXP008e3 model has about 15–25 per cent more power than  $\Lambda$ CDM at all scales and source redshifts, a signature of its growth rate being maintained over the whole redshift range. As obtained by the tomographic analysis performed by Pace et al. (2015), where only the ratio of the power spectra for sources at redshift  $z_s = 2$  and  $z_s = 1$  has been considered, we confirm that the small differences they find at very high  $l$  in the coupled models, and particularly in the bouncing model SUGRA003, are actually present and are much clearer in our high-resolution ray-traced maps. The same behaviour of the power spectra we find has also been noticed and discussed by Carbone et al. (2013) using ray-tracing technique to compute the CMB lensing maps; however also Carbone et al. (2013) are not able to resolve the small-scale features of the cDE–DM models because the angular resolution on their maps is more than a factor of 10 lower than ours.

Clearly, WL tomography, i.e. the study of the WL signal as a function of the source redshift, can be an important tool for studying these differences in the evolution of structure with redshift that occur in different cDE models. Fig. 5 shows this more clearly. In the left-hand panel, we display the ratio between the convergence power spectrum computed at five different source redshifts and the one computed for sources located at  $z_s = 0.5$ ; line styles and colours are the same as in Fig. 4. For EXP003 and EXP008e3, the ratios tend to lie above the  $\Lambda$ CDM one, but for SUGRA003 it stays below. This is a result of structures in the SUGRA003 model evolving less rapidly at late times while in the EXP003 and EXP008e3 models they evolve more rapidly. The difference between the models is most evident at small scales as a consequence of non-linear structure formation. The right-hand panel of Fig. 5 shows the rescaled cross-spectra between the convergence at different redshifts within the same light-cone. High correlation indicates that the lensing is being caused by the same objects. Interestingly, SUGRA003 has more correlations at small scales and less at large scales, while the other models have the opposite trend, due to an enhancement of their growth rate at high redshifts and to a depletion at low redshifts with respect to the  $\Lambda$ CDM one. We remind the reader that the growth rate in EXP003 and EXP008e3 is always enhanced with respect to the standard model causing a higher  $\sigma_8$  at the present time.

The pixel resolution of our maps (8.8 arcsec in all cases) will have some impact on the accuracy of the lensing statistics calculated. In particular, the pixelation tends to smooth out peaks and reduce the power on small scales (Takahashi et al. 2011; Pace et al. 2015). To investigate how our pixelation might be affecting the results we constructed the pixel probability distribution function (PDF) of the convergence map as shown in Fig. 6 for one realization of the  $\Lambda$ CDM model with sources at  $z_s = 1.4$ . The different line styles and colour histograms show the PDF when the original map has been pixel-degraded by a factor of 2, 4 and 8 – see the figure caption for more details. It can be seen that increasing the

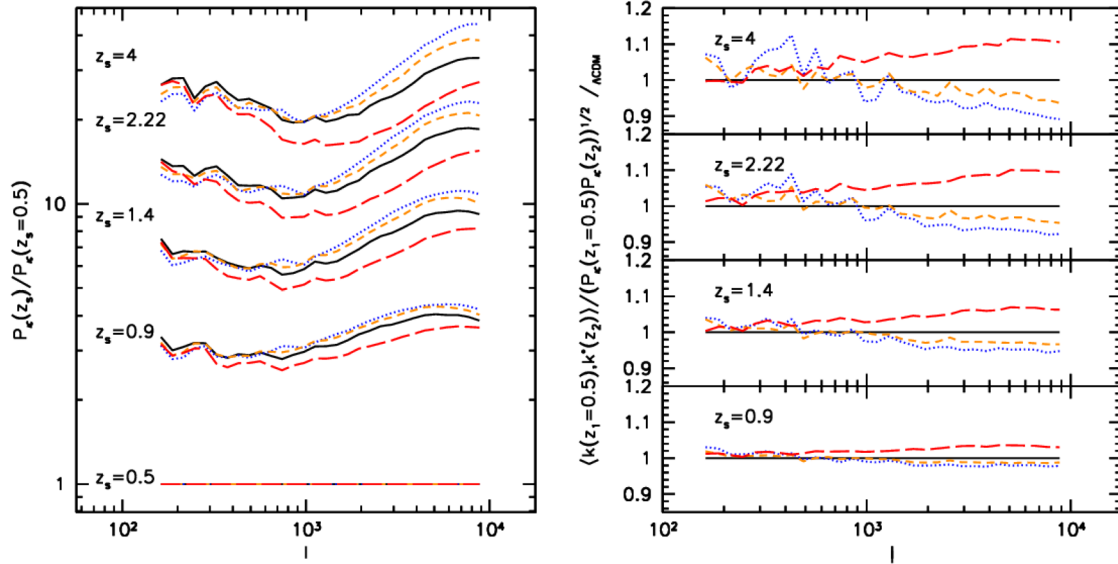


**Figure 5.** Left-hand panel: ratio between the convergence power spectrum computed at different source redshifts – as indicated in the labels – and the one at  $z_s = 0.5$  for each cosmological model. Right-hand panel: rescaled cross-power-spectra between redshift  $z = 0.5$  and  $z_2$  – as indicated in the labels – for the different models, computed from the lensing maps. All the cross-spectra have been rescaled with respect to the  $\Lambda$ CDM prediction. This is why the correlation parameter on the right can be greater than one. Different line styles and colours are as in Fig. 4.

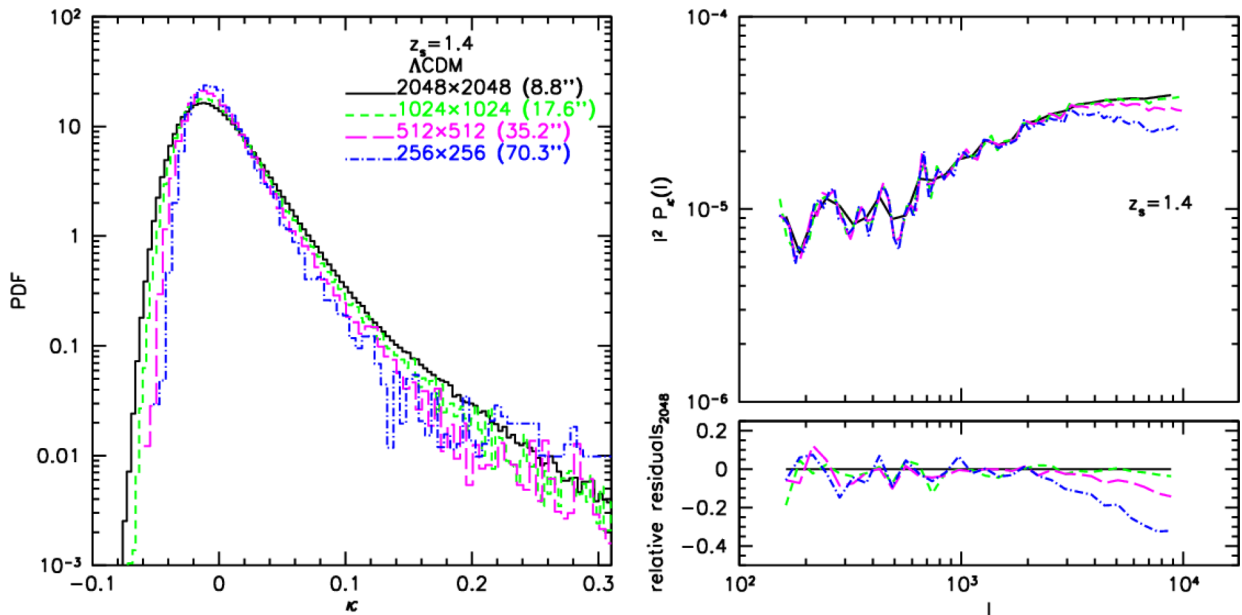


**Figure 6.** Left-hand panel: histograms of the convergence values in one realization of the  $\Lambda$ CDM model, considering sources at  $z_s = 1.4$ . The solid black histogram shows the case for the map resolution used throughout this paper (8.8 arcsec pixels). The short dashed green, long dashed magenta and dot-dashed blue histograms show the PDF of the maps degraded by a factor of 2, 4 and 8, respectively. Right top panel: convergence power spectra of these maps. Right bottom panel: the ratios of the power spectra with different resolutions with respect to the highest resolution one.

pixel size reduces the number of very high and very low  $\kappa$  pixels as expected. The impact this has on the convergence power spectrum is shown in the right-hand panel of Fig. 6, where the power spectra for different resolutions are plotted. In the bottom right-hand panel are the relative residuals with respect to the original, highest resolution map. These figures show that reducing the map resolution by a factor of 2 causes small differences of only a few per cent in the power spectrum relative to the original map for  $l \lesssim 5 \times 10^3$ . The discrepancies become larger for the maps degraded by a factor of 4 and 8. We conclude that our calculations

are not affected by pixelation for  $l \lesssim 5 \times 10^3$  above few per cent level.

It has been shown in this section that the evolution of the density power spectrum in different cDE models will cause significant changes to the convergence power spectrum as a function of source redshift. These differences from  $\Lambda$ CDM can be positive or negative at a particular source redshift and they can be scale dependent. In the following sections, we will investigate some other statistics that might be observationally more practical in terms of direct measurements and noise estimations.

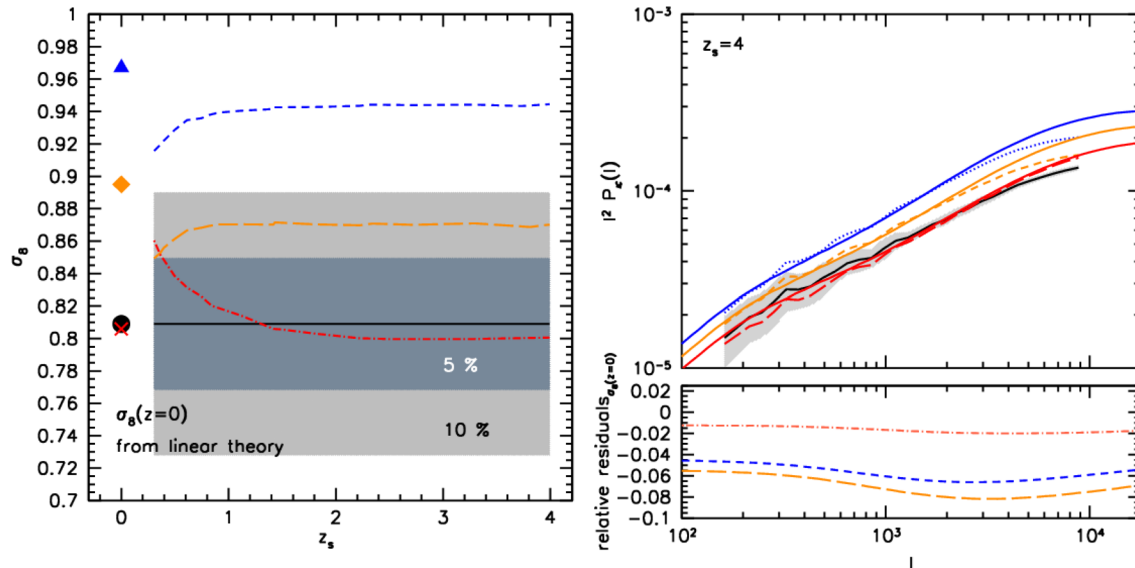


**Figure 7.** Left-hand panel:  $\sigma_8$  as a function of the source redshift, obtained by fitting the corresponding convergence power spectrum for each cosmological model, fixing the total mass density parameter  $\Omega_m$  to its true value in the simulation. The coloured points show the value of  $\sigma_8$  at the present time interpolated from linear theory: blue triangle (EXP003), orange diamond (EXP008e3), red cross (SUGRA003) and black dot ( $\Lambda$ CDM). Right top panel: convergence power spectra for sources at redshift  $z_s = 4$  as measured from the light-cones in the four cosmological models. As in previous figures solid, dotted, dashed and dot–dashed lines correspond to  $\Lambda$ CDM, EXP003, EXP008e3 and SUGRA003, respectively. The corresponding solid coloured curves represent the best  $\Lambda$ CDM power spectra obtained fixing the total matter content and varying  $\sigma_8$ . Bottom right panel: the ratio between the convergence power spectrum with the best  $\sigma_8$  and the one obtained using  $\sigma_8(z=0)$ , i.e. the interpolated value using linear theory (Baldi 2012c) is shown for the three cDE models.

#### 4.1.1 Impact on the measured normalization of the power spectrum for sources at different redshifts

As noted previously, the coupled DM–DE models affect both the power spectrum normalization and the small-scale non-linear behaviour of structure formation when compared with the  $\Lambda$ CDM model. One way to see this is through the impact on measurements of the power spectrum normalization. The power spectrum normalization will be quantified by the standard  $\sigma_8$  parameter which is the variance of the mass overdensity density within a sphere of radius  $8h^{-1}$  Mpc at redshift zero with only the linear evolution of the power spectrum taken into account. When  $\sigma_8$  is measured using data at redshifts larger than zero a correction factor that is cosmology dependent must be applied to translate the normalization to  $z = 0$ . If the underlying cosmology assumed in doing this procedure is the correct one then  $\sigma_8$  will not depend on the source redshift. In this section, we investigate what would happen if a  $\Lambda$ CDM cosmology is assumed while the true cosmology corresponds to one of our cDE models. This exercise will help us gain some insight on when during cosmic history these models leave most of their imprints on the lensing power spectrum.

The left-hand panel of Fig. 7 shows the recovered  $\sigma_8$  values as a function of the different source redshifts for the four cosmological models while assuming  $\Lambda$ CDM. We measure  $\sigma_8$  integrating the non-linear power spectrum (see e.g. Lewis et al. 2000; Takahashi et al. 2012) up to the different considered source redshifts assuming the  $\Lambda$ CDM model; in this way the  $\sigma_8$  value is directly related to the measurement of the growth factor associated to a  $\Lambda$ CDM universe. Line styles and colours are the same as in Fig. 4, the shaded light grey and grey regions indicate 5 and 10 per cent accuracies in the measurement of  $\sigma_8$  for the  $\Lambda$ CDM case. Also shown are the true  $\sigma_8$  values – interpolated using linear theory (Baldi 2012c) – for each model. In the case of  $\Lambda$ CDM, the correct value is recovered, but in the other models incorrect  $\sigma_8$  values are recovered and they change

as a function of source redshift. Such behaviour would therefore signal a failure of the underlying  $\Lambda$ CDM assumption. In EXP003 and EXP008e3,  $\sigma_8$  is underestimated, while the opposite is true in SUGRA003 for some of the source redshift range. These trends are due to the different evolution of the growth factor and of the Hubble function in the coupled DM–DE models – see figs 1 and 2 in Baldi (2012c). It is interesting to note that for the three coupled models we never obtain the value of  $\sigma_8$  interpolated from linear theory at the present time. This means that when fitting the convergence power spectrum of the coupled DM–DE models both projection effects and non-linearities contribute to the measured  $\sigma_8$ .

In the right-hand panel of Fig. 7, we show the measured convergence power spectrum in the different light-cone simulations for sources at  $z_s = 4$  – solid, dotted, dashed and dot–dashed refer to  $\Lambda$ CDM, EXP003, EXP008e3 and SUGRA003, respectively. For the three coupled DM–DE models, we display best-fitting theoretical convergence power spectra obtained by assuming we live in a  $\Lambda$ CDM universe. In the bottom panel, we present the relative deviation of the theoretical convergence power spectrum computed with the best  $\sigma_8$  and the one linearly interpolated from theory at  $z = 0$ . While for SUGRA003 model, the relative deviation is of the order of 1–2 per cent, for both EXP003 and EXP008e3 it manifests larger values.

These results indicate that, if sufficient accuracy is attained, measuring  $\sigma_8$  from shear maps as a function of redshift would lead to inconsistencies were one of these cDE models the correct one. To observe these effects will require large amounts of very accurate data of the kind that will be provided by future wide surveys, like the Euclid space mission (Laureijs et al. 2011). An additional complication not taken into account here is that WL studies are generally sensitive to a combination of the power spectrum normalization,  $\sigma_8$ , and the total density of matter,  $\Omega_m$ , in the combination  $\sigma_8(\Omega_m/0.25)^\alpha$  where  $\alpha$  is dependent on the WL statistic used:  $\alpha = 0.46, 0.53$

and 0.64, for the shear two-point correlation function, the shear in a top-hat or aperture mass, respectively (Fu et al. 2008; Kilbinger et al. 2013, see also a more extended discussion in the next section). However,  $\Omega_m$  is likely to be well constrained by other observations such as the CMB.

#### 4.2 Other weak lensing statistics

Other statistics of the convergence field besides the power spectrum may help to probe the non-Gaussian nature of the PDF of gravitational lensing observables. In particular, statistics like the variance and the skewness in a top-hat or compensated filter represent interesting tools to constrain cosmological parameters and the DE evolution as a function of redshift (Fu et al. 2008; Kilbinger et al. 2013; Kitching et al. 2014). In this context, multiplane lensing simulations are important tools to compute the predicted variance and skewness of the shear or convergence field, both for standard and non-standard models. In particular, the skewness in aperture is somehow independent of the normalization of the power spectrum and represents a strong indicator of the evolution of  $\Omega_m$  as a function of redshift (Schneider et al. 1998).

The interpretation and modelling of the lensing signals due to large-scale structures requires a precise understanding of the high-order statistics of the lensing field (Sato et al. 2009). Several cosmological analyses have been done by studying the mass aperture variance and the skewness as a function of the smoothing angle  $\theta$ , adopting a top-hat or a compensated aperture filter. These measured quantities have the advantage that they can be directly compared with the theoretical predictions extracted from the convergence power spectrum. However, a good model of the signal on small scales, where the non-linear effects start to dominate, is of fundamental importance to interpreting observational data. Since the top-hat shear rms between different CoDECS models, but only at  $z_s = 1$ , has been studied by Pace et al. (2015), we will present and discuss in this section the aperture–mass dispersion and the associated skewness for three different source redshifts.

The variance of the filtered shear field as a function of the filter size contains the same information as the power spectrum, but the filter can be made to have compact support and additional practical advantages (Sato & Nishimichi 2013). They can also have a different sensitivity to the cosmological model and be particularly dependent

on non-linear structure formation. In addition, the skewness and higher order statistics can be easily defined and interpreted for the filtered shear field. We will investigate a particular choice of filter called the compensated aperture filter:

$$Q_\theta(\vartheta) = \frac{6}{\pi\theta^2} \left( \frac{\vartheta}{\theta} \right) \left( 1 - \frac{\vartheta^2}{\theta^2} \right) \quad (9)$$

with support  $\vartheta = [0, \theta]$ . In Fourier space, it is

$$W_{\text{ap}} = \frac{\sqrt{276}J_4(\xi)}{\xi^2} \quad (10)$$

as Fourier counterpart (Harnois-Déraps, Vafaei & Van Waerbeke 2012). It has the attractive property of being well localized in Fourier space near wavenumber  $l \sim 5/\theta$ . We apply this filter in Fourier space with zero padding to reduce boundary effects. Since the average value of the convergence on each plane is zero, the variance across the map, typically indicated as  $\langle M_{\text{Ap}}^2 \rangle$ , can be computed from the convergence power spectrum performing the following integral:

$$\langle k^2 \rangle_{\text{Ap}} = \langle M_{\text{Ap}}^2 \rangle = \frac{1}{(2\pi)^2} \int dl l P_\kappa(l) W_{\text{Ap}}^2(l\theta). \quad (11)$$

Similarly, it is possible to define the large-scale structure noise (Hoekstra 2003) adopting a different compensated filter (see Appendix A for more discussion about this).

In Fig. 8, we show the variance of the convergence field as a function of the smoothing scale  $\theta$  with this filter. The different line styles and colours refer to the four considered cosmological models and the shaded grey region encloses the rms of the measurement performed in the different realizations of the  $\Lambda$ CDM light-cones. The measurements are presented for three source redshifts:  $z_s = 0.5$ , 1.4 and 4. The bottom panels show the relative residuals of the measurements in the different coupled models with respect to the  $\Lambda$ CDM ones. We notice that the variance of the measurement in the  $\Lambda$ CDM model decreases as a function of the source redshift, as expected from the evolution of the clustering of the dark matter in the Universe. While at low redshifts, the Universe is more clustered and so we may trace rays through clusters and voids – enhancing the variance of the measurements in different realizations, at high redshifts the Universe is more homogenous and so the variance through different realizations is expected to be smaller, as we confirmed in Fig. 8.

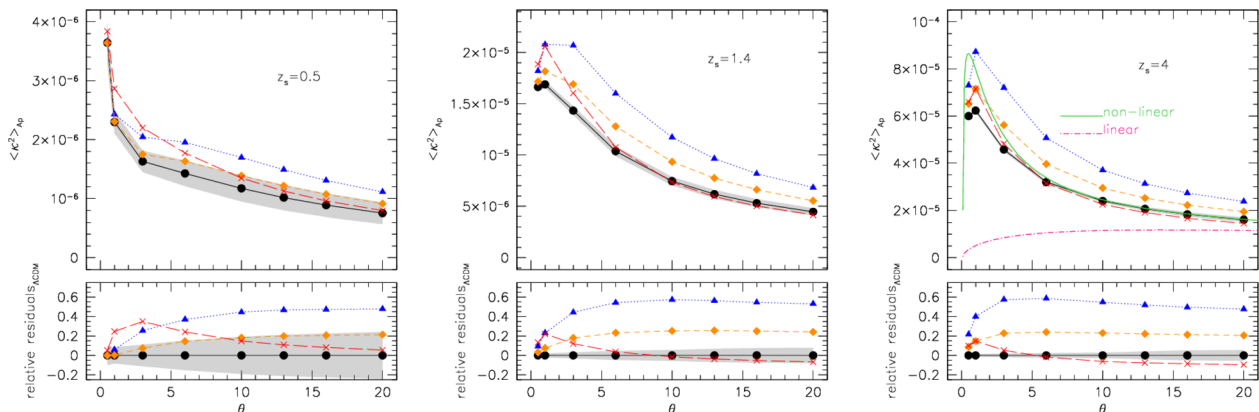


**Figure 8.** Top panels: variance of the convergence field smoothed with a compensated aperture filter as a function of the smoothing scale  $\theta$ , for sources at three different redshifts:  $z_s = 0.5, 1.4$  and  $4$ , from left to right. Bottom panels: relative residuals as a function of the smoothing scale with respect to the measurements in the  $\Lambda$ CDM model. The grey shaded region represents the rms of the variance computed on the different realizations of the  $\Lambda$ CDM light-cone. In the right-hand panel, for sources at  $z_s = 4$ , we also show predictions from linear and non-linear theory. For the other source redshifts, the agreement is analogous to this one.

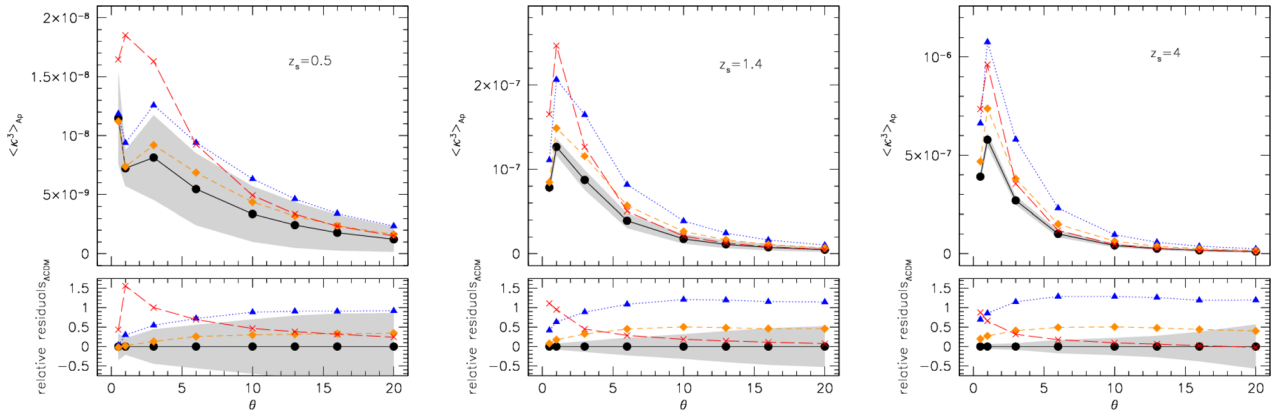


**Figure 9.** As Fig. 8, but for skewness of the convergence field.

To demonstrate how much of this signal depends on non-linear structure formation, we show  $\langle M_{\text{Ap}}^2 \rangle$  calculated with only the linear power spectrum in the right-hand panel of Fig. 8 for  $z_s = 4$  in the  $\Lambda$ CDM model. It can be seen that non-linear structure formation has a dominant role below  $\theta \simeq 20$  arcmin.

The agreement between non-linear theoretical predictions and our simulations for  $\Lambda$ CDM is quite good aside from limitations in the simulations at small scales due to numerical mass and force resolution limitations. As with the power spectrum, the deviations from  $\Lambda$ CDM in Fig. 8 are positive for EXP003 and EXP008e3 (by about 50 and 20 per cent – as for the convergence power spectrum). For SUGRA003,  $\langle M_{\text{Ap}}^2(\theta) \rangle$  is larger than for  $\Lambda$ CDM at small  $\theta$  and becomes smaller at large scales mirroring the behaviour in Fig. 4. This trend is a consequence of a slightly lower  $\sigma_8$  governing the large  $\theta$  behaviour while for small scales the boost in variance comes from differences in the structure of haloes: in SUGRA003 haloes are more concentrated and have more substructures mainly at low redshifts (as was shown e.g. by Giocoli et al. 2013).

The filtered variance’s strong dependence on non-linear structure leads one to think that the skewness of the filtered convergence map might be a good discriminator between models. The skewness is plotted in Fig. 9 as a function of  $\theta$ , for all the cosmological models, and once again for three source redshifts. As in the case of the variance, the measurements in the EXP003 and EXP008e3 cosmologies are larger than those in  $\Lambda$ CDM, but with the relative residuals that are a factor of 2 larger than for the variance. In addition, for large angles the relative residuals between  $\Lambda$ CDM and SUGRA003 are very small but increase for small  $\theta$ , a signature of the higher small-scale clustering present in this case, the high concentration of haloes and their clumpiness. For a fixed angular scale, the difference becomes larger for smaller source redshift owing to the build up of non-linear structure at late times in the SUGRA003 model. These differences between models are more evident here than for the variance.

In Fig. 10, we show the variance (left) and the skewness (right) of the convergence field as a function of the source redshift while fixing the scale of the filter to 6 arcmin which is comparable to the typical scale of the central region of galaxy clusters at

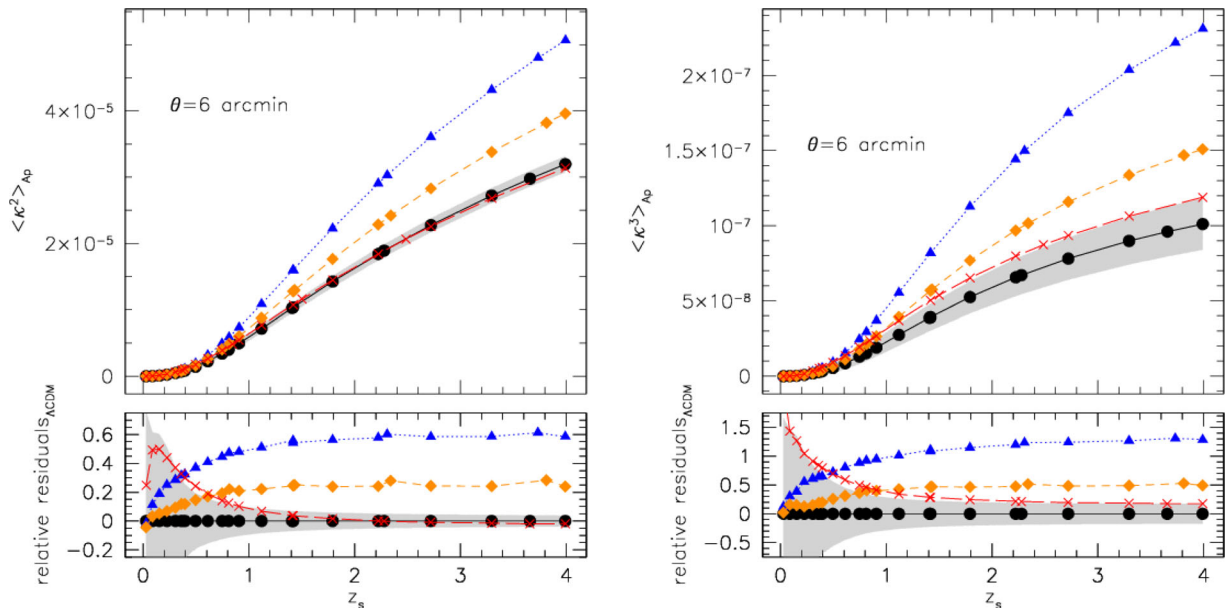


**Figure 10.** Variance (left-hand panel) and skewness (right-hand panel) of the convergence field smoothed with a compensated aperture filter with  $\theta = 6$  arcmin as a function of the source redshifts. The bottom panels show the relative residuals of the variance and the skewness with respect to the  $\Lambda$ CDM measurements. The shaded grey region represents the rms of the moments computed on the different realizations of the  $\Lambda$ CDM light-cones.

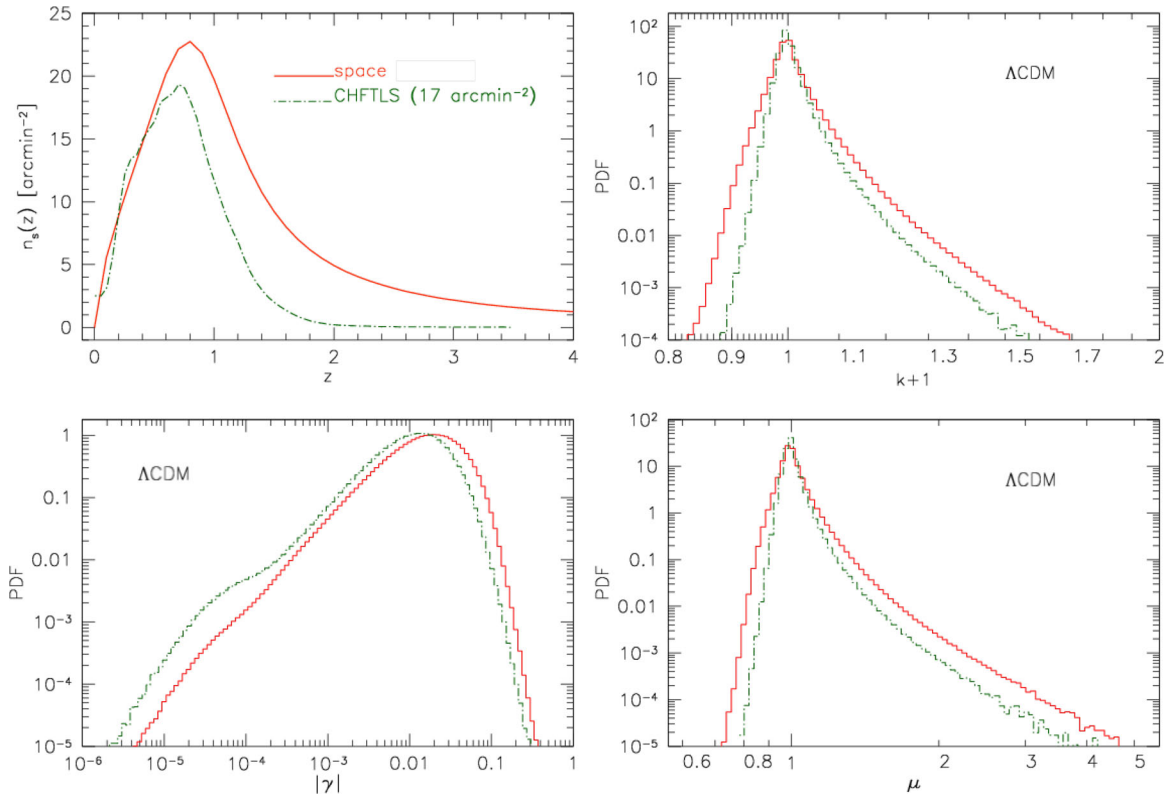


**Figure 11.** Top left: source redshift distribution expected for space- and ground-based observations. Top right, bottom left and bottom right PDF of convergence, shear and magnification extracted from the 25  $\Lambda$ CDM light-cones randomly sampled eight times with the corresponding source redshift distribution. The various colour and line style histograms refer to the different considered cosmologies (see Fig. 4), the shaded grey region encloses the rms of the measurement performed in the different light-cone realizations in the  $\Lambda$ CDM model.

intermediate redshifts. The bottom panels again show the residuals of the measurements with respect to  $\Lambda$ CDM. Both the variance and the skewness grow as a function of the source redshifts because of the increased path-lengths and the additional structure along the paths. For  $z_s > 0.5$ , all the models tend to present a constant bias with respect to  $\Lambda$ CDM: positive in EXP003 and EXP008e3 while almost vanishing in the bouncing model SUGRA003. Note that the relative difference in the skewness is almost double than in the variance. While the behaviour of the bouncing model SUGRA003 is within the rms of the  $\Lambda$ CDM measurements, the EXP003 and EXP008e3 are quite distinct with a positive bias of about 60 and 20 per cent for the variance and 120 and 50 per cent for the skewness for  $z_s > 0.5$ .

The behaviour of the variance and skewness of the filtered convergence field highlights the possibility of using sources at different redshifts and with different smoothing scales to investigate the coupling between the dark components of the universe.

### 4.3 Probability distribution function from source redshift distributions

In previous sections, we have discussed the results for the variance and the skewness of the convergence field for sources located at different fixed redshifts. In this last section, we explore the one-point distribution function of convergence, shear and magnification given instead a source redshift distribution. We do this in order to understand whether the simple one-point statistics of the lensing field, and which source redshift distribution can help us to understand the non-Gaussian nature of the fields in the different cosmological

models. In our analysis, we consider two different source redshift distributions that typically correspond to a ground- and a space-based WL survey. For the ground-based case, we adopt the source density as a function of redshift as computed by Kilbinger et al. (2013) – the data points are publicly available on the CFHTLenS webpage<sup>1</sup> – while for the space based we consider the parametrization adopted by Boldrin et al. (2012) which has been extracted from a Euclid-like observation of the Hubble Ultra Deep Field performed with the code SKYLENS (Meneghetti et al. 2008). In the top left panel of Fig. 11, we show the two adopted source redshift distribution normalizing the CFHTLS one to have a total density of sources of about 17 galaxies per  $\text{arcmin}^2$ . What is most evident about the two is that the high-redshift tail in the space-based observation extends to higher redshifts while in the ground-based case there are almost no galaxies above  $z = 2$ . In order to extract the convergence and shear catalogues from one light-cone realization, we proceed in the following way: (i) given a source redshift distribution we compute the number of expected sources in a redshift interval  $dz$  that corresponds to the difference in comoving distance between two source planes; (ii) for each  $dz$  we randomly assign to each source both a redshift and an angular position in the field of view. We do not take into account any clustering of the sources which should not be important for our purpose. The corresponding lensing quantity (convergence or shear) is then linearly interpolated in redshift considering the values computed between two consecutive planes at the corresponding angular position of the source. The other panels of

<sup>1</sup> <http://www.cfhtlens.org/astromers/cosmological-data-products>

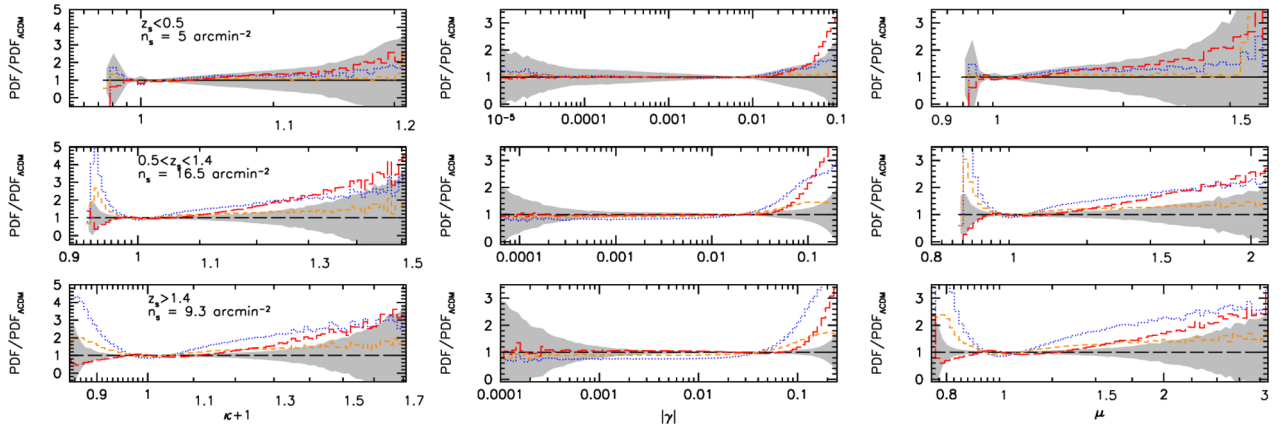


**Figure 12.** PDFs of convergence (left-hand column), shear (central column) and magnification (right-hand column) extracted from the light-cones of the different cosmologies rescaled with respect to the  $\Lambda$ CDM one, assuming a space-based source redshift distribution. Rows refer to different intervals for the source redshifts:  $z_s < 0.5$ ,  $0.5 < z_s < 1.4$  and  $z_s > 1.4$ , from top to bottom. Each light-cone has been randomly sampled eight times with the according source redshift distribution.

Fig. 11 show the convergence, shear and WL magnification for the different  $\Lambda$ CDM light-cone realizations, each randomly sampled 25 times with the according  $n(z_s)$ . From the figure, we notice that because the two adopted source redshift distributions have different shapes, mainly in the intermediate- and high-redshift tail, the one-point lensing statistics from the same simulated light-cones tend to be different. While the shape of the convergence and the magnification are broadened going from ground- to space-based observations, the shear distribution is shifted towards larger values.

In Fig. 12, we show the expected convergence, shear and magnification probability distributions assuming a space-based source redshift distribution for the four cosmologies, rescaled with respect to the  $\Lambda$ CDM one. In comparison to Pace et al. (2015), we notice that our distributions are realistically more extended in the high-value tails because of the different way adopted in doing the ray tracing, and of the larger resolution with which the maps are resolved. While in Fig. 6 by Pace et al. (2015), the one-point statistic manifests itself mainly in the different initial power spectrum normalization of the coupled models, in Fig. 12 it is possible to observe also a more pronounced distinction in the high-value tails. Particularly, in both the PDF of the convergence and the magnification, the small-scale clustering and the high halo concentration in SUGRA003 model raise the high-value distribution tails. This is also evident in the shear distributions where both SUGRA003 and EXP003 are well outside the rms of the  $\Lambda$ CDM distribution for  $\gamma > 0.075$ . The situation is different for the corresponding PDF extracted from the same light-cones considering a ground-based source redshift distribution, not shown here. First, we notice that the source densities in the intermediate- and the high-redshift bins reduce to 11.2 and 0.8  $\text{arcmin}^{-2}$ , respectively, and that the SUGRA003 model is enclosed within the rms of the  $\Lambda$ CDM for large values. In this case only EXP003 appears distinguishable from  $\Lambda$ CDM. The signature of enhanced high-redshift growth in the considered models is much less distinguishable with the ground-based lensing survey than it is with a space-based survey, as also discussed in Beynon et al. (2012).

In Fig. 13, we display the variance of the convergence field computed from different light-cone realizations in three redshift bins for a space- (left) and ground-based (right), assuming a CFHTLS source redshift distribution. Black, blue, orange and red colours refer to the  $\Lambda$ CDM, EXP003, EXP008e3 and SUGRA003 models, respectively. In each panel, we also show with a green solid line the noise level in the three redshift bins related to the intrinsic

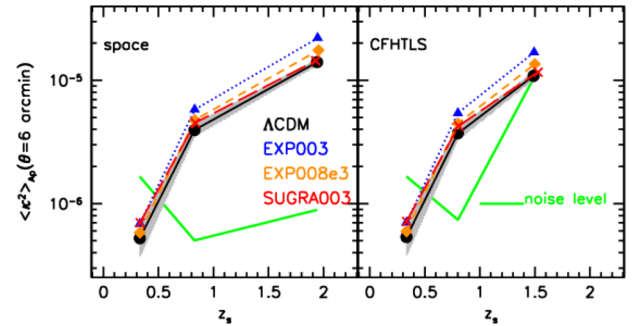


**Figure 13.** Variance of the convergence field computed within the different light-cone realizations and cosmologies adopting a space and a ground-based (CFHTLS) source redshift distribution. Different data points and colours are the same as in Fig. 10. The solid (green) line represents the corresponding noise level associated to the intrinsic galaxy ellipticity distribution and the source number density. This noise level is for a 25  $\text{deg}^2$  field.

ellipticity distribution  $\sigma_\epsilon = 0.25$  and to the corresponding source number density  $n_g$  contained in the aperture filter (Schneider et al. 1998; van Waerbeke 2000). This is the noise for a 25  $\text{deg}^2$  field. Neglecting systematic errors, the noise for a larger survey will go down by roughly a factor of 1 over the square root of the survey area. From this plot, it can be seen that a ground-based survey will have difficulty distinguishing between the models, but that a survey like Euclid would be expected to clearly distinguish between them.

## 5 SUMMARY AND CONCLUSIONS

Several studies have been conducted to understand which observables are most suitable to investigate cDE cosmologies (Beynon et al. 2012; Giocoli et al. 2013; Carbone et al. 2013; Pace et al. 2015). Our aim here was to extend the ray-tracing analyses of Carbone et al. (2013) and Pace et al. (2015) by investigating whether a tomographic slicing of the background sources within high-resolution-simulated light-cones might provide additional information to distinguish cDE models from the standard  $\Lambda$ CDM cosmology and possibly the different cDE models from each other. Our main results can be summarized as following:

- (i) While the convergence power spectra in the EXP003 and EXP008e3 models present only a higher normalization with respect

to the  $\Lambda$ CDM model, the power spectrum in the SUGRA003 model exhibits a more complex behaviour. Compared to  $\Lambda$ CDM, in this model structure formation progresses rapidly at high redshift and slows down at low redshift, resulting in a comparable value of  $\sigma_8$  at  $z = 0$  once the normalization is fixed using the CMB. The large-scale behaviour of the convergence power spectrum reflects the slower growth at low redshifts and it is weakly suppressed. This suppression is due to the change of sign of the drag term in this class of cDE models, which are characterized by a ‘bounce’ of the DE scalar field whose motion changes direction (see Baldi 2012a, for a detailed discussion of bouncing cDE). In the non-linear regime, this effect determines a faster collapse of bound structures that results in a higher average concentration of haloes and in a larger abundance of substructures (see e.g. the discussion in Giocoli et al. 2013). This is reflected in an enhancement of the convergence power spectrum at small angular scales – large  $l$ .

(ii) The coupling between the dark components can also be seen in the lensing signals as a function of source redshifts. In particular, if  $\sigma_8$  is measured from the convergence power spectrum, assuming  $\Lambda$ CDM and fixing  $\Omega_m$  in the fitting, the result will change as a function of source redshift in cDE cosmologies, i.e. they will be inconsistent with  $\Lambda$ CDM.

(iii) The cross-correlation between the convergence for different source redshifts is significantly enhanced in the SUGRA003 model while it is slightly suppressed in the EXP003 and the EXP008e3 models relative to what is expected in  $\Lambda$ CDM, this because of the high concentration and the high small-scale clustering that manifest as consequence of the high- and low-redshift-enhanced and suppressed growth rate that characterize the SUGRA003 model.

(iv) The aperture mass statistic also exhibits signs of the coupling between dark matter and DE. In particular for  $\theta > 5$  arcmin and sources  $z_s > 1$  EXP003 and EXP008e3 differ by about 50 and 20 per cent, respectively, as compared to  $\Lambda$ CDM. The skewness of a compensated aperture, measuring the non-Gaussian nature of the convergence field, also reflects differences between the various models, specifically the higher level of dark matter clustering in the SUGRA003 model is evident for small filtering scales.

(v) The different models analysed in the work also result in distinct PDF of the lensing signals – convergence, shear and magnification – extracted from a space-based source redshift distribution. The various models not only manifest differences in the intermediate values, as discussed by Pace et al. (2015), but also in the high-value tails.

Therefore, it emerges from the analyses performed in this work that the differences between the coupled dark matter–DE models and the standard CDM can be explained not only in terms of the different normalizations of the linear matter power spectrum but also in terms of the distinct halo properties and small-scale clustering that characterize the dark matter component. These manifest themselves in different WL observables at small angular scales and also in the one-point statistics taken in different redshift bins, given a space-based source redshift distribution that extends to high redshifts. In particular, in this last case, both SUGRA003 and EXP003 models appear to be easily distinguishable from  $\Lambda$ CDM by future WL surveys.

## ACKNOWLEDGEMENTS

We thank the anonymous referee for her/his useful comments that help to improve the presentation of our results. CG thanks CNES for its financial support. CG and RBM’s research is part of the

project GLENCO, funded under the European Seventh Framework Programme, Ideas, Grant Agreement n. 259349. MB acknowledges support by the Marie Curie Intra European Fellowship ‘SIDUN’ within the 7th Framework Programme of the European Commission. We acknowledge financial contributions from contracts ASI/INAF I/023/12/0 and by the PRIN MIUR 2010–2011 ‘The dark Universe and the cosmic evolution of baryons: from current surveys to Euclid’. CG, MB and LM also acknowledge the financial contribution by the PRIN INAF 2012 ‘The Universe in the box: multiscale simulations of cosmic structure’. We also thank Cosimo Fedeli, Federico Marulli, Michele Moresco and Mauro Roncarelli for useful discussions. GC thank Giulia Despali, Giuseppe Tormen and Vincenzo Mezzalana to have host part of the computer jobs run to perform the ray tracing.

## REFERENCES

- Amara A. et al., 2012, *MNRAS*, 424, 553  
 Bahé Y. M., McCarthy I. G., King L. J., 2012, *MNRAS*, 421, 1073  
 Baldi M., 2012a, *MNRAS*, 420, 430  
 Baldi M., 2012b, *MNRAS*, 422, 1028  
 Baldi M., Viel M., 2010, *MNRAS*, 409, L89  
 Baldi M., Pettorino V., Robbers G., Springel V., 2010, *MNRAS*, 403, 1684  
 Baldi M., Pettorino V., Amendola L., Wetterich C., 2011a, *MNRAS*, 418, 214  
 Baldi M., Lee J., Macciò A. V., 2011b, *ApJ*, 732, 112  
 Bartelmann M., 1996, *A&A*, 313, 697  
 Bartelmann M., 2010, *Classical and Quantum Gravity*, 27, 233001  
 Bartelmann M., Schneider P., 2001, *Phys. Rep.*, 340, 291  
 Becker M. R., 2013, *MNRAS*, 435, 115  
 Bellagamba F., Maturi M., Hamana T., Meneghetti M., Miyazaki S., Moscardini L., 2011, *MNRAS*, 413, 1145  
 Benjamin J. et al., 2013, *MNRAS*, 431, 1547  
 Bernstein G. M., Jarvis M., 2002, *AJ*, 123, 583  
 Beynon E., Baldi M., Bacon D. J., Koyama K., Sabiu C., 2012, *MNRAS*, 422, 3546  
 Boldrin M., Giocoli C., Meneghetti M., Moscardini L., 2012, *MNRAS*, 427, 3134  
 Brax P. H., Martin J., 1999, *Phys. Lett. B*, 468, 40  
 Bridle S. et al., 2010, *MNRAS*, 405, 2044  
 Carbone C., Baldi M., Pettorino V., Baccigalupi C., 2013, *J. Cosmol. Astropart. Phys.*, 009, 004  
 Cui W., Baldi M., Borgani S., 2012, *MNRAS*, 424, 993  
 Fedeli C., Semboloni E., Velliscig M., Van Daalen M., Schaye J., Hoekstra H., 2014, *J. Cosmol. Astropart. Phys.*, 008, 028  
 Fu L. et al., 2008, *A&A*, 479, 9  
 Giocoli C., Moreno J., Sheth R. K., Tormen G., 2007, *MNRAS*, 376, 977  
 Giocoli C., Meneghetti M., Bartelmann M., Moscardini L., Boldrin M., 2012, *MNRAS*, 421, 3343  
 Giocoli C., Marulli F., Baldi M., Moscardini L., Metcalf R. B., 2013, *MNRAS*, 434, 2982  
 Giocoli C., Meneghetti M., Metcalf R. B., Ettori S., Moscardini L., 2014, *MNRAS*, 440, 1899  
 Harnois-Déraps J., Vafaei S., Van Waerbeke L., 2012, *MNRAS*, 426, 1262  
 Harnois-Déraps J., van Waerbeke L., Viola M., Heymans C., 2015, *MNRAS*, 450, 1212  
 Heymans C., Rowe B., Hoekstra H., Miller L., Erben T., Kitching T., van Waerbeke L., 2012, *MNRAS*, 421, 381  
 Heymans C. et al., 2013, *MNRAS*, 432, 2433  
 Hilbert S., White S. D. M., Hartlap J., Schneider P., 2008, *MNRAS*, 386, 1845  
 Hildebrandt H. et al., 2012, *MNRAS*, 421, 2355  
 Hoekney R. W., Eastwood J. W., 1988, *Computer Simulation using Particles*. Hilger, Bristol  
 Hoekstra H., 2003, *MNRAS*, 339, 1155  
 Hoekstra H., Hartlap J., Hilbert S., van Uitert E., 2011, *MNRAS*, 412, 2095

- Hoekstra H., Mahdavi A., Babul A., Bildfell C., 2012, *MNRAS*, 427, 1298
- Jullo E., Kneib J.-P., Limousin M., Elfarsdóttir Á., Marshall P. J., Verdugo T., 2007, *New J. Phys.*, 9, 447
- Kacprzak T., Zuntz J., Rowe B., Bridle S., Refregier A., Amara A., Voigt L., Hirsch M., 2012, *MNRAS*, 427, 2711
- Kaiser N., 1992, *ApJ*, 388, 272
- Kaiser N., Squires G., 1993, *ApJ*, 404, 441
- Kaiser N., Squires G., Broadhurst T., 1995, *ApJ*, 449, 460
- Kilbinger M., 2014, preprint ([arXiv e-prints](#))
- Kilbinger M. et al., 2013, *MNRAS*, 430, 2200
- Kitching T. D. et al., 2014, *MNRAS*, 442, 1326
- Kitching T. D., Heavens A. F., Das S., 2015, *MNRAS*, 449, 2205
- Kneib J.-P., Natarajan P., 2011, *A&AR*, 19, 47
- Komatsu E. et al., 2011, *ApJS*, 192, 18
- Kowalski M. et al., 2008, *ApJ*, 686, 749
- Lacey C., Cole S., 1993, *MNRAS*, 262, 627
- Laureijs R. et al., 2011, preprint ([arXiv e-prints](#))
- Lewis A., Challinor A., Lasenby A., 2000, *ApJ*, 538, 473
- Lucchin F., Matarrese S., 1985, *Phys. Rev. D*, 32, 1316
- Mandelbaum R., Seljak U., Cool R. J., Blanton M., Hirata C. M., Brinkmann J., 2006, *MNRAS*, 372, 758
- Marulli F., Baldi M., Moscardini L., 2012, *MNRAS*, 420, 2377
- Maturi M., Meneghetti M., Bartelmann M., Dolag K., Moscardini L., 2005, *A&A*, 442, 851
- Meneghetti M., Bartelmann M., Dolag K., Moscardini L., Perrotta F., Bacigalupi C., Tormen G., 2005, *A&A*, 442, 413
- Meneghetti M. et al., 2008, *A&A*, 482, 403
- Merten J., Cacciato M., Meneghetti M., Mignone C., Bartelmann M., 2009, *A&A*, 500, 681
- Merten J. et al., 2015, *ApJ*, 806, 4
- Metcalfe R. B., Petkova M., 2014, *MNRAS*, 445, 1942
- Miller L. et al., 2013, *MNRAS*, 429, 2858
- Moresco M., Marulli F., Baldi M., Moscardini L., Cimatti A., 2014, *MNRAS*, 443, 2874
- Navarro J. F., Frenk C. S., White S. D. M., 1996, *ApJ*, 462, 563
- Navarro J. F. et al., 2004, *MNRAS*, 349, 1039
- Oguri M., Bayliss M. B., Dahle H., Sharon K., Gladders M. D., Natarajan P., Hennawi J. F., Koester B. P., 2012, *MNRAS*, 420, 3213
- Okabe N., Takada M., Umetsu K., Futamase T., Smith G. P., 2010, *PASJ*, 62, 811
- Pace F., Baldi M., Moscardini L., Bacon D., Crittenden R., 2015, *MNRAS*, 447, 858
- Perlmutter S. et al., 1999, *ApJ*, 517, 565
- Petkova M., Metcalfe R. B., Giocoli C., 2014, *MNRAS*, 445, 1954
- Planck Collaboration XVI, 2013, *A&A*, 571, A16
- Refregier A., Rhodes J., Groth E. J., 2002, *ApJ*, 572, L131
- Refregier A. et al., 2004, *AJ*, 127, 3102
- Riess A. G. et al., 1998, *AJ*, 116, 1009
- Roncarelli M., Moscardini L., Borgani S., Dolag K., 2007, *MNRAS*, 378, 1259
- Sato M., Nishimichi T., 2013, *Phys. Rev. D*, 87, 123538
- Sato M., Hamana T., Takahashi R., Takada M., Yoshida N., Matsubara T., Sugiyama N., 2009, *ApJ*, 701, 945
- Schmidt B. P. et al., 1998, *ApJ*, 507, 46
- Schneider P., van Waerbeke L., Jain B., Kruse G., 1998, *MNRAS*, 296, 873
- Schrabback T. et al., 2010, *A&A*, 516, A63
- Semoloni E., Hoekstra H., Schaye J., 2013, *MNRAS*, 434, 148
- Sereno M., Giocoli C., Ettori S., Moscardini L., 2015, *MNRAS*, 449, 2024
- Smith R. E. et al., 2003, *MNRAS*, 341, 1311
- Springel V., 2005, *MNRAS*, 364, 1105
- Springel V. et al., 2005, *Nature*, 435, 629
- Suzuki N. et al., 2012, *ApJ*, 746, 85
- Takahashi R., Oguri M., Sato M., Hamana T., 2011, *ApJ*, 742, 15
- Takahashi R., Sato M., Nishimichi T., Taruya A., Oguri M., 2012, *ApJ*, 761, 152
- Tormen G., 1998, *MNRAS*, 297, 648
- van Waerbeke L., 2000, *MNRAS*, 313, 524
- von der Linden A. et al., 2014a, *MNRAS*, 439, 2
- von der Linden A. et al., 2014b, *MNRAS*, 443, 1973
- Wetterich C., 1988, *Nucl. Phys. B*, 302, 668
- Zitrin A., Broadhurst T., Barkana R., Rephaeli Y., Benítez N., 2011, *MNRAS*, 410, 1939

## APPENDIX A: LARGE-SCALE STRUCTURE NOISE IN CLUSTER SHEAR PROFILES

The results obtained in this paper can also be used to evaluate how the level of noise produced by the large-scale structure on the estimates of galaxy cluster masses from WL data (Bahé, McCarthy & King 2012; Hoekstra et al. 2012; Merten et al. 2015; Giocoli et al. 2014; Sereno et al. 2015; von der Linden et al. 2014a,b) are dependent on the cosmological background.

Several algorithms have been developed to invert the lens equation and derive the cluster's projected mass (Jullo et al. 2007; Merten et al. 2009; Zitrin et al. 2011). Since galaxy clusters have a matter distribution that on average can be described by a well-defined density profile (Navarro, Frenk & White 1996; Navarro et al. 2004), a direct way to weight them is to fit the (spherically binned) measured shear profile adopting the corresponding theoretical prediction (Bartelmann 1996; Giocoli et al. 2012).

However, the light travelling from sources located behind a galaxy cluster is deflected not only by cluster matter distribution, but also by all the matter it encounters along its trajectory. This uncorrelated matter density distribution contributes to the lensing signal, and affects the shear measurements (Schneider et al. 1998; Hoekstra 2003; Hoekstra et al. 2011).

This lensing noise, which depends on the source redshift and on the angular size  $\theta$  of the annulus we are looking at, can be computed analytically from the convergence power spectrum adopting the formalism developed by Hoekstra (2003):

$$\sigma_{\text{LSS}}^2(\theta) = \frac{1}{2\pi} \int dl l P_{\kappa}(l) J_2^2(l\theta), \quad (\text{A1})$$

where  $J_2$  represents the second-order Bessel function and is a particular choice of the aperture mass statistic averaged over an annulus ranging from  $(\theta - \delta\theta/2)$  to  $(\theta + \delta\theta/2)$ .

In Fig. A1 we show, for the four considered cosmologies, the noise produced by the Large Scale Structures (LSS) on spherically averaged shear profiles. The results are presented for three typical scales ( $\theta=1, 10$  and  $20$  arcmin) and considering sources up to redshift  $z_s = 4$ . As already done in the case of the aperture mass statistics, the results are directly extracted from the convergence maps that have been smoothed using the appropriate  $J_2$  kernel.

From the figure, we notice that the noise produced by large-scale structures is higher in the cDE models with respect to the  $\Lambda$ CDM cosmology. This is particularly true for the EXP003 and EXP008e3 models: for  $\theta > 10$  arcmin and for sources with  $z_s > 0.5$  they present values that are about 20 and 10 per cent larger than the one measured in the  $\Lambda$ CDM model, respectively. For the SUGRA003 model, a smaller increase of noise is evident only for  $\theta = 1$  arcmin and/or for sources at low redshift. We underline also that the rms of the measurement  $\Lambda$ CDM decreases as a function of redshifts because of a combination of (i) the choice filter, (ii) the field of view and (iii) the clustering of the haloes as a function of redshifts – at high redshift the universe is more homogenous.

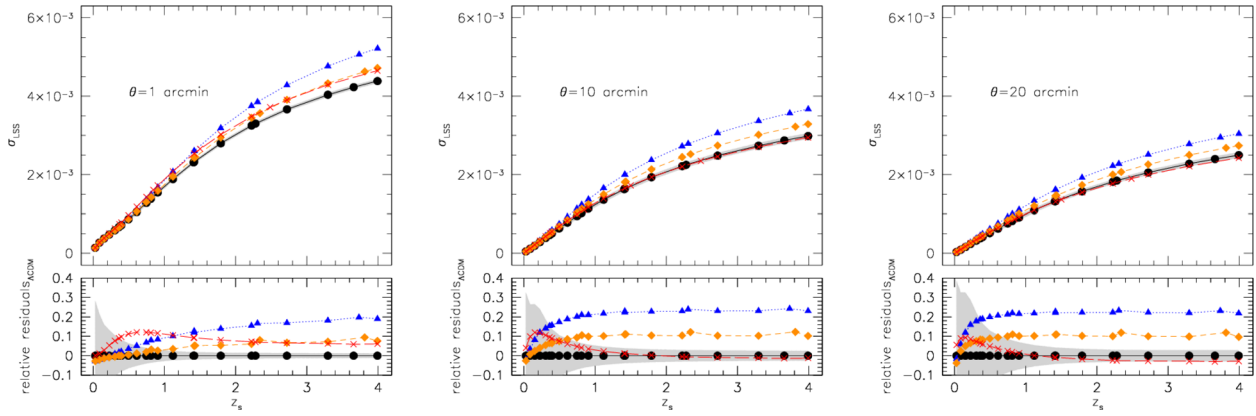


**Figure A1.** Large-scale structure noise computed adopting a particular choice of the aperture mass statistic, averaged over an annulus ranging from  $(\theta - \delta\theta/2)$  to  $(\theta + \delta\theta/2)$ , as a function of the source redshift measured from the convergence maps extracted of the light-cones of the four considered CoDECS simulations. Left-hand, central and right-hand panel refer to different angular scales  $\theta$ ; colours and line styles are as in Fig. 8.

This paper has been typeset from a  $\text{\TeX}/\text{\LaTeX}$  file prepared by the author.